



Human iPSC-derived neurons reveal early developmental alteration of neurite outgrowth in the late-occurring neurodegenerative Wolfram syndrome

Sandra Pourtoy-Brasselet, Axel Sciauvaud, Maria-Gabriela Boza-Moran,
Michel Cailleret, Margot Jarrige, H  l  ne Polv  che, J  r  me Polentes, Eric
Chevet, C  cile Martinat, Marc Peschanski, et al.

► To cite this version:

Sandra Pourtoy-Brasselet, Axel Sciauvaud, Maria-Gabriela Boza-Moran, Michel Cailleret, Margot Jar-
rige, et al.. Human iPSC-derived neurons reveal early developmental alteration of neurite outgrowth
in the late-occurring neurodegenerative Wolfram syndrome. *American Journal of Human Genetics*,
2021, 108 (11), pp.2171-2185. 10.1016/j.ajhg.2021.10.001 . hal-03409417

HAL Id: hal-03409417

<https://hal.science/hal-03409417>

Submitted on 22 Nov 2021

HAL is a multi-disciplinary open access archive for the deposit and dissemination of scientific research documents, whether they are published or not. The documents may come from teaching and research institutions in France or abroad, or from public or private research centers.

L'archive ouverte pluridisciplinaire **HAL**, est destinée au dépôt et à la diffusion de documents scientifiques de niveau recherche, publiés ou non, émanant des établissements d'enseignement et de recherche français ou étrangers, des laboratoires publics ou privés.



Distributed under a Creative Commons Attribution - NonCommercial 4.0 International License

Human iPSC-derived neurons reveal early developmental alteration of neurite outgrowth in the late-occurring neurodegenerative Wolfram syndrome

* **Corresponding author:** Laetitia Aubry, laubry@istem.fr

ABSTRACT:

Recent studies indicate that neurodegenerative processes that appear during childhood and adolescence in individuals with Wolfram syndrome (WS) occur in addition to early brain development alteration, which is clinically silent. Underlying pathological mechanisms are still unknown. We have used induced pluripotent stem cell-derived neural cells from individuals affected by WS in order to reveal their phenotypic and molecular correlates. We have observed that a subpopulation of Wolfram neurons displayed aberrant neurite outgrowth associated with altered expression of axon guidance genes. Selective inhibition of the ATF6 α arm of the Unfolded Protein Response prevented the altered phenotype, although acute endoplasmic reticulum stress response -which is activated in late Wolfram degenerative processes- was not detected. Among the drugs currently tried in individuals with WS, valproic acid was the one that prevented the pathological phenotypes. These results suggest that early defects in axon guidance may contribute to the loss of neurons in individuals with WS.

INTRODUCTION

Wolfram syndrome (WS, OMIM 222300) is a rare multi-systemic monogenic disease which is characterized by a panel of symptoms appearing during childhood and adolescence¹. Focal neurodegenerative processes then occur, affecting neurosensory systems and the brainstem. Recent results of magnetic resonance imaging studies have revealed, however, that individuals affected by Wolfram syndrome display in addition a statistically significant overall reduction of brain volume. The origin of the brain volume reduction has been ascribed to yet unknown neurodevelopmental defects²⁻⁴ since it is present as early as the authors looked for it, and remains stable, in contrast to the later-appearing neurodegenerative processes that progress over time. This finding could be read in conjunction with older analyses of brains from WS affected persons that had pointed out widespread axonopathy⁵ or diffuse leukoencephalopathy⁶ in the absence of clinical correlates.

The molecular mechanisms that underlie WS, which results from mutations in *WFS1* gene (OMIM 606201) and consequently with the loss of wolframin protein, have been mainly ascribed to a defect in the stress response of the endoplasmic reticulum (ER)^{7; 8}. This is supported by the localization of wolframin at the ER membrane⁹ and its role as an inhibitor of the ATF6 α branch of the Unfolded Protein Response¹⁰ (UPR). Accordingly, its absence in pancreatic β cells from individuals affected by WS has been associated with a defective control of the UPR leading to cell dysfunction and death¹¹, and diabetes. Defects in the ER stress response have also been proposed as the main pathological mechanism that lead to the progressive neurodegenerative processes that affect retinal ganglionic neurons and, by extension, sensory neurons of the ear and brainstem that also display strong losses over time¹². Such phenomena were, however, difficult to reconcile with the spatial and temporal features of the overall reduction in brain volume.

In the present study, we sought to investigate the cellular and molecular mechanisms associated with the neurodevelopmental pathology in WS. We hypothesized that neurons differentiated from induced pluripotent stem (iPS) cells would provide us with a directly relevant experimental model in order to compare early neurodevelopmental phenomena from healthy

and Wolfram donors. Protocols for the differentiation of pluripotent stem cells based upon the dual inhibition of both the activin/nodal and BMP pathways, the two canonical Smad-dependant pathways, have been shown to recapitulate nicely the progression of cells along the neural lineage^{13; 14}. In particular, glutamatergic cortical neurons can be specifically differentiated¹⁵. This has thus allowed us to compare similar neuronal populations from healthy and Wolfram donors at discrete early stages of neural development and reveal pathological abnormalities that provide clues to understand the mechanisms that lead to the defects in brain volume identified in individuals with WS.

MATERIAL AND METHODS

Fibroblast reprogramming and pluripotent stem cell culture

The CT1 and CT3 control iPSC lines have been reprogrammed at I-Stem and already published^{15; 16} (CT1 corresponding to line 1869 and CT3 to line PB12). CT2 iPSC line was reprogrammed from IMR-90 lung fibroblast cell (ATCC® CCL-186). WS1 and WS2 iPSC lines were kindly given by the New York Stem Cell Foundation and have already been published¹⁷. WS5 iPSC line was derived from fibroblasts provided by Dr Cécile Delettre and the late Pr Christian Hamel, isolated from one individual affected by WS biopsy after approval of the local ethical committee (NCT03853252, Institute for Neurosciences in Montpellier, France). All the cell lines used for this study as well as the experimental processes have been performed according to the French legal policy. Consequently, informed consent was obtained from all participants or their legal representatives.

Fibroblasts were grown in fibroblast culture medium consisting of DMEM high glucose (Invitrogen), GlutaMAX™ Supplement (Invitrogen), supplemented with 10% fetal bovine serum (FBS, Sigma-Aldrich), 1% non-essential amino acids (Invitrogen) and 1 mM sodium pyruvate (Invitrogen). CT2 and WS5 iPSC lines were obtained and characterized as described by Yu et al.¹⁸ using Addgene plasmid 20925, 20926 and 20927. iPSCs were grown on MEFs in hESCs culture medium consisting of DMEM with 20% KSR, 1% non-essential amino acids, 1% Glutamax, 0.1% β -mercaptoethanol and 0.1% penicillin / streptomycin (all from ThermoFisher

Scientific) and supplemented with 10 ng/mL FGF-2 (Peprotech) with manual passaging once a week and daily medium change during the characterization steps. They were then adapted for feeder-free culture and grown on vitronectin-coated dishes (ThermoFisher Scientific) in StemMACS™ iPS-Brew XF (Miltenyi Biotec). Cultures were fed every two days and passaged every 5-7 days.

Pluripotent stem cell differentiation

For embryoid bodies (EBs) differentiation, iPSC colonies growing on MEFs were detached with 1 mg/mL collagenase (ThermoFisher Scientific) during 10 minutes at 37°C, resuspended in hESCs medium without FGF-2 and cultured in low attachment 6-well plates for 7 days at 37°C and 5% CO₂. The EBs were then plated on 0.1% gelatin-coated (Sigma-Aldrich) plates and maintained for another 7 days prior immunostaining.

Neural stem cells (NSCs) differentiation was performed as described previously ¹⁵. At this stage of differentiation, cells can be frozen in a 90% foetal bovine serum / 10% dimethylsulfoxide ≥99.5% (DMSO, 0.005%, VWR) solution. After thawing, cells were seeded on a poly-L-ornithin / laminin (PO/LAM) coated support, in N2B27 medium consisting of DMEM/F12, neurobasal, N2 and B27 supplements, 0.1% β-mercaptoethanol and 0.1% penicillin / streptomycin (all from ThermoFisher Scientific) supplemented with 10 ng/mL of FGF-2 and EGF (Peprotech) and 10 μM of Y-27632 (Stemcell Technologies). Medium was changed the next day without Y-27632 and then changed every two days. NSCs were passaged twice a week using Trypsin-EDTA 0.05 % (ThermoFisher Scientific) and seeded on PO/LAM-coated support at a density of 50,000 cells/cm² for amplification.

Neuronal differentiation was induced by plating the NSCs at low density (50,000 cells/cm²) in PO/LAM-coated culture plates in N2B27 medium without FGF-2 and EGF. At day 4, 10 μM DAPT (R&D Systems) was added to the medium to stop cell proliferation. The medium was changed every 4 days and neurons were obtained after 18-21 days of *in vitro* (DIV) differentiation.

Drug treatments

For drug treatments experiments, NSCs were differentiated into neurons as previously described. The neurons were treated twice at DIV 10 and DIV 14 with the following molecules and concentrations ¹⁹: 10 μ M ceapin-A7 (Sigma-Aldrich); 2.5 μ M MKC-8866 (Medinnovata); 10 μ M salubrinal (Sigma-Aldrich); 100 nM liraglutide (Bio-Techne); 10 μ M dantrolene (Sigma-Aldrich); 1 mM 4-phenyl butyric acid (4PBA, Merck); 0.5 mM or 1.5 mM valproic acid (VPA, Sigma-Aldrich). Ceapin-A7, MKC-886, salubrinal, liraglutide, and dantrolene were resuspended in DMSO. For further analyses, cultures were stopped at DIV 18. Neuraminidase (NM) at 10 mU (Sigma-Aldrich) was used as a technical control to prevent the fasciculation as this enzyme removes specifically sialic acid residues and consequently reduces non-specifically adhesion between neurites ²⁰.

Ion ampliseq transcriptome human gene expression kit

For each of the 12 samples, 50 ng of total RNA was reverse transcribed using the Ion AmpliSeq Transcriptome Human Gene Expression kit following the protocol of the manufacturer (Thermofisher Scientific) ²¹. The cDNA libraries were amplified and barcoded using Ion AmpliSeq Transcriptome Human Gene Expression core panel and Ion Xpress Barcode Adapter (Thermofisher Scientific). The amplicons were quantified using Agilent High Sensitivity DNA kit before the samples were pooled in sets of eight. Emulsion PCR and enrichment was performed on the Ion OT2 system Instrument using the Ion PI Hi-Q OT2 200 kit (Thermofisher Scientific). Samples were loaded on an Ion PI v3 Chip and sequenced on the Ion Proton System using Ion PI Hi-Q sequencing 200 kit chemistry (200 bp read length; Thermofisher Scientific). The Ion Proton reads (FASTQ files) were imported into the RNA-seq pipeline of Partek Flow software (v6 Partek Inc) using hg19 as a reference genome. The number of reads per sample was ranging from 7.1 million to 10 million reads. To determine genes that are differentially expressed between groups mapped reads were quantified using Partek E/M algorithm after normalization by the Total count/sample (the resulting counts represent the gene expression levels on reads/millions for over 20,800 different genes present in the

AmpliSeq Human Gene Expression panel). Differentially expressed genes were identified using Partek Gene Specific Analysis (GSA) algorithm. Gene lists were filtered at $p\text{value} \leq 1\%$; $|\text{Fold Change}| \geq 1.5$ minReads100. The use of $p\text{value}$ instead of adjusted $p\text{value}$ is justified by biological meaning and experimental validations (Figure S4C) ²². Biological interpretations of the list of differentially expressed genes were performed using dedicated software (Partek Genomics Suite (v6.6), and the web-based gene list enrichment analysis tool EnrichR ^{23; 24}). EnrichR analysis were performed on KEGG2016 data base and GO biological process 2017b. Ampliseq data produced in this study have been deposited on NCBI GEO under the accession number GSE156911.

Time-lapse imaging of neuronal differentiation

NSCs were seeded at 50,000 cells/cm² in PO/LAM-coated 384-well culture plates in N2B27 medium to induce neuronal differentiation. The plates were incubated in an IncuCyte Zoom Live Cell Imaging System (Essen Bioscience) and phase contrast images were automatically taken under 10X microscopic magnification every 4 hours for the first two weeks of differentiation and then every 12 hours for the next two weeks. Pictures were extracted and piled up using the IncuCyte Zoom Software to create the movies.

WS5 rescued (WS5R) iPSC line generation

WS5R line was generated by CRISPR-Cas9-mediated knock-in to introduce *WFS1* cDNA, under a doxycycline inducible promoter, at the AAVS1 locus. As the backbone, we used the pAAVS1-PDi-CRISPRn (Addgene #73500) plasmid. The Cas9 cassette was replaced with *WFS1* cDNA of the *WFS1*-pcDNA3 plasmid (Addgene#13011) by using Gibson Assembly. This vector includes homology arms at the 5' and 3' regions immediately flanking the DNA sequence of AAVS1 locus to specifically direct integration of the vector into the AAVS1 locus. This plasmid is mainly composed of rtTA under pCAG promoter, PuroR under control of T2A peptide and inducible TR3G promoter that allows the expression of *WFS1* with doxycycline treatment.

For the WS5 rescue cell line generation, the WS5 iPS cells were first transfected with the linearized plasmid using Lipofectamine® 3000 (ThermoFisher Scientific). Cells were transfected a second time with the *in vitro* preformed Cas9 nuclease/gRNA RNP (Integrated DNA Technologies, IDT) using Lipofectamine™ CRISPRMAX™ (ThermoFisher Scientific). The dual transfection has been realized following the manufacturer protocols.

The RNP complex formation was performed using the T2 guide RNA (IDT) that target AAVS1 locus: (GGGGCCACTAGGGACAGGAT) that was complexed with spCas9 Protein (ratio 1.2/1) during 10 minutes at room temperature before the transfection. The clones were selected after one week of culture with StemMACS™ iPS-Brew XF (Miltenyi Biotec) medium and 200 ng/mL puromycin (ThermoFisher Scientific). WS5R iPSCs were differentiated into NSCs and neurons. In order to induce the production of wolframin, NSCs were treated with 50 ng/mL doxycycline (Sigma-Aldrich) at each medium change during 10 days. The 50 ng/mL doxycycline treatment was then maintained all along the differentiation into neurons.

Immunocytochemistry

Cells were fixed with 4% paraformaldehyde (Electron Microscopy Sciences) for 15 minutes at room temperature. Cells were then placed in a blocking buffer (phosphate-buffered saline, 2% bovine serum albumin and 0.1% Triton X-100). Primary antibodies were diluted in blocking buffer and applied overnight at 4 °C. Secondary antibodies conjugated to Alexa fluorophores (ThermoFisher Scientific) were diluted at 1:1000 in blocking buffer and applied for 1 hour at room temperature in the dark. Hoechst 33258 (Sigma-Aldrich) diluted at 1:3000 was applied in the same time to visualize the cell bodies. The cells were visualized on a Zeiss inverted fluorescence microscope and image acquisition was performed using the Zen Blue software (Zeiss). When higher resolution was necessary, confocal imaging was performed using a Zeiss LSM880-Airyscan Confocal Microscope driven by the Zeiss Zen black software. The antibodies used are described in Table S2.

Immunostaining quantifications

Three biologically independent differentiations for each conditions were investigated and 5 images at 20X magnification per each differentiation were quantified. Due to the high number of fibers on each image, the neurites thickness quantification was approached using a method of unbiased random sampling in ImageJ/FIJI. The method was based on the use of a grid (area per point: 8,000 μm^2) apposed automatically on the image by the software. A random third of the squares composing the grid were quantified for each image. On each counted square of the grid, neurite thickness was measured manually using the selection tool of imageJ to delimitate the diameter of each fiber. ImageJ was then asked to measure the corresponding line length (i.e. the fiber thickness). The results for each image were then compiled on a global table to be classified in 3 arbitrary thickness intervals (0 – 3 μm ; 3 – 6 μm ; > 6 μm). The same data were used to analyse the mean thickness of the neuronal network for each condition.

To quantify the proportions/percentages of positive cells for each labelling, the CellInsight CX7 High-Content Screening (HCS) Platform and the HSC Studio software (ThermoFisher Scientific) were used. Based on the CX7-Colocalization Bioapplication and the acquisition of images at 10X magnification, a homemade algorithm had allowed the individual detection and quantification of nuclei (Hoechst), HuC/D (green) and CUX2 (red), and finally the calculation of the proportion of each labelling to the total number of cells, as quantitative readouts.

mRNA extraction and Reverse-Transcription (RT) PCR

Total RNA samples were isolated using the RNeasy Mini or Micro Plus extraction kit and QIAcube instrument (Qiagen) according to the manufacturer's protocol. RNA quantification and quality were assessed using the NanoDrop ND-1000 spectrophotometer (ThermoFisher Scientific) and the ND V33.7.1 software. The cDNA samples were synthesized from 500 ng of RNA with SuperScript III reverse transcriptase (ThermoFisher Scientific) using a mix of 500 ng/ μL random primers (ThermoFisher Scientific) and 500 ng/ μL Oligo(dT) (ThermoFisher Scientific).

Quantitative PCR (qPCR)

Quantitative PCR assay were performed with Luminaris HiGreen qPCR Master Mix, low ROX (ThermoFisher Scientific) using the QuantStudio 12K Flex Real-Time PCR System (ThermoFisher Scientific), with hold stage (50°C for 2 minutes and 95°C for 10 minutes) followed by 40 cycles of denaturation (95°C for 15 seconds) and annealing (60°C for 1 minute). Quantification of gene expression was based on the $2^{-\Delta\Delta C_t}$ method and normalized to 18S expression. Primers listed in Table S3 were used for gene expression.

Thapsigargin treatment

NSCs were seeded at 75,000 cells/cm² on PO/LAM coated 6 well plates in N2B27 medium supplemented with 10 ng/mL of EGF and FGF-2 and incubated at 37°C, 5% CO₂ overnight. The next day, cells were treated with the non-competitive inhibitor of the sarco/endoplasmic reticulum Ca²⁺ ATPase (SERCA) 50 nM thapsigargin (TG, Sigma-Aldrich). The cells were collected using RLT+ lysis buffer (Qiagen) after 4 hours, 6 hours and 8 hours of treatment. For each time point, the control condition of DMSO was collected.

***XBP1* gel analysis**

RNA extraction and RT were performed as described above. For the *XBP1* splicing analysis, a PCR amplification was carried out with 0.05 U/μL recombinant Taq DNA polymerase (ThermoFisher Scientific) and the primers listed in Table S3. The amplification was performed using a first step at 95°C for 5 minutes followed by 30 cycles of denaturation (60 seconds at 95°C), followed by annealing step (30 seconds at 59°C) and finish by elongation step (30 seconds at 72°C), in the Eppendorf® Mastercycler. The PCR products (spliced *XBP1* (*XBP1s*) and unspliced *XBP1* (*XBP1u*) respectively at 193 pb and 223 pb) were quantified using the BioAnalyzer 2100 and the Agilent DNA 1000 kit (Agilent) according to the manufacturer's protocol. Spliced *XBP1* expression was normalized to total *XBP1* (*XBP1s* + *XBP1u*).

Western immunoblotting

Proteins samples were isolated from cell-lysates using RIPA buffer (Sigma-Aldrich) supplemented with 1% protease inhibitors cocktail (Sigma-Aldrich) and 10% phosphatase inhibitor (Roche). Samples quantification was performed using Pierce® BCA protein assay kit (ThermoFisher Scientific) with CLARIOstar Plus instrument (BMG Labtech). The samples were prepared at a concentration of 30 µg of proteins and were placed 10 minutes at 70°C. Proteins were loaded on 4-12% Nu-PAGE® Bis-Tris gels (ThermoFisher Scientific) with the Chameleon® Duo Pre-stained Protein Ladder (Li-Cor) and migrated during 10 minutes at 50 mA and 40 minutes at 100 mA. The gels were then transferred onto nitrocellulose membranes (ThermoFisher Scientific) using the iBlot 2 Dry Blotting System (ThermoFisher Scientific). Blots were blocked for 1 hour at room temperature in Odyssey® Blocking Buffer (Li-Cor) and then incubated with primary antibody in the blocking buffer with 0.2% TWEEN 20 (Sigma-Aldrich) overnight at 4°C. Blots were then incubated with fluorescent secondary antibodies (1:10 000, Li-Cor) in the blocking buffer with 0.2% TWEEN 20 (Sigma-Aldrich) in the dark at room temperature for 1 hour. The blots were revealed using Odyssey CLx Imaging System (Li-Cor). The antibodies used are described in Table S2.

Statistical Analysis

All data were graphed and analyzed using GraphPad Prism 5 (GraphPad Software). Data shown are the mean \pm s.e.m. Student's t-tests were used for comparison between two groups. Group differences were analyzed with one-way analysis of variance (ANOVA) followed by Dunnett's multiple comparisons test.

RESULTS

Six human iPS cell lines were used in this study, three derived from healthy controls (CT1, CT2 and CT3) and three derived from individuals affected by WS with genetically and clinically identified Wolfram syndrome (WS1, WS2 and WS5). Information on CT and WS iPSCs are summarized in Table S1. All cell lines were validated using classical assays for stemness, pluripotency and genomic integrity (Figure S1A, B and C). WS proliferating neural

stem cells (NSCs) and post-mitotic neurons showed an absence of wolframin protein unlike all CT cells (Figure 1 and Figure S1E).

WS neurons display impaired neurite outgrowth

When CT and WS cell lines were differentiated along the neural lineage, no difference in term of detection of the NSCs markers, NESTIN and SOX2, and that of the cortical neurons markers, HuC/D and CUX2, as well as the total number of cells, was observed between both types of lines (Figure 1A, B, C, and Figure S1D). In contrast, TUJ1 immunostaining in neurites revealed a striking morphological difference between CT and WS cells. Indeed, CT neurons formed a typical stellate array of thin branching fibers whereas WS cells exhibited long and large processes (up to several millimeters in length) without apparent branching (Figure 2A and Figure S2A, D). Using confocal microscopy, these large processes appeared to be formed by the aggregation of parallel neurites bundled together (Figure 2B). Live-cell imaging revealed that those abnormal neurite figures appeared between days 10 and 14 of neuronal differentiation *in vitro* (DIV), depending on the cell line (supplemental movies A, B, C and D). In WS neuronal cultures, neuritic bundles built up progressively while neurites were growing straight through the culture without apparent interaction with cell clusters. Processes grew longer and larger over about a week, after which the neuritic networks remained stable. In addition, the growing tips of some of the neuritic bundles formed unusual U-turns and even full circles (Figure S2B).

As a way to quantify the phenomenon, we measured the thickness of isolated and bundled neurites in CT and WS cultures. Although most of the above-mentioned structures were below 3 μm in size in both CT and WS cells, WS cells exhibited a smaller number of those thin processes than CT. Conversely, the number of neurites bundles were both more abundant and larger in WS cells, reaching up to 58 μm in width while CT neuritic structures did not exceed 12 μm . Consequently, the mean thickness of neuritic structures was higher in WS neurons than in the CT (Figure 2C). To further compare WS and CT cells, we defined three thickness intervals (0 to 3 μm , 3 to 6 μm , and > 6 μm) and observed that >90% of the CT

neuritic structures ranged in the 0 to 3 μm interval while this proportion was significantly reduced to about 80% in WS cells (Figure 2D and Figure S2C). Conversely, there was less than 1% neuritic structures per mm^2 with a thickness $> 6 \mu\text{m}$ in CT whereas this number was up to 10% in WS cells (Figure 2D, E and Figure S2C). These results indicate that the absence of wolframin leads to aberrant neurite outgrowth which in turn could impact on neural functionality.

Restoration of wolframin normalizes neurite outgrowth in WS neurons

To confirm that the absence of wolframin was involved in the neuritic phenotype, a *WFS1*-rescued WS iPS cell line was generated using CRISPR/Cas9 gene-editing to introduce the *WFS1* cDNA under a doxycycline-inducible promoter at the AAVS1 locus (the WS5 line was used; Figure 3A). Pluripotent characteristics and normal karyotype were maintained in the rescued iPS cell line (WS5R) (Figure S3A, B). Successful gene editing was confirmed after 50 ng/mL doxycycline (Dox) treatment as wolframin synthesis was detected in NSCs and neurons (Figure 3B). WS5R cells differentiated similarly to the parental WS5 line into NSCs (Figure S3C). Moreover, expression of *WFS1* upon treatment with 50 ng/mL Dox did not alter the percentage of HuC/D+ and CUX2+ neurons (Figure 3C, D), thus indicating that the initial properties of the cell line were not altered by the expression of the transgene. In sharp contrast, Dox-mediated induction of *WFS1* expression changed the neuritic network (Figure 3E), restoring it to what was observed in CT cells. Typical stellate arrays of thin neurites extending between clusters of cells were observed in the Dox-treated cultures. Quantification of isolated and bundled neurites per mm^2 showed a normalization of the profile that closely resembled CT cultures (Figure 3G, H and Figure S3D). We observed similar results for the mean thickness (Figure 3F). As a control, doxycycline treatment in non-engineered WS5 neurons did not affect markers of differentiation and was also ineffective on neuritic outgrowth (Figure S3E, F, G), demonstrating that the normalization of the neuritic network by doxycycline treatment required the presence of the *WFS1* construct.

WS cells exhibit defects in the expression of genes involved in neurodevelopment and axon guidance

Global gene expression was compared between CT and WS NSCs and neurons. In a principal component analysis (PCA), the samples clustered based on their phenotype (CT NSCs, WS NSCs, CT neurons and WS neurons) (Figure 4A). In contrast, the two groups CT and WS differed in the number of differentially expressed genes (DEGs) ($P\text{value} \leq 1\%$; $\text{Fold Change} \geq 1.5$; $\text{minReads} \geq 100$). There were 493 DEGs for WS compared to CT NSCs (249 upregulated and 244 downregulated) and 254 DEGs for neurons WS, in comparison to CT neurons (87 upregulated and 167 downregulated). Among these DEGs, 29 were commonly dysregulated in WS NSCs and neurons (Figure S4A). When DEGs in neurons were mapped to Kyoto Encyclopedia of Genes and Genomes (KEGG) pathways, the most significantly enriched pathway was “axon guidance” (Figure 4B). Functional annotation revealed that the top three significantly enriched gene ontology categories were “neurogenesis”, “nervous system development” and “axon guidance” (Figure 4B). In WS cells, axon growth and guidance-related genes were either upregulated, like roundabout-1 (*ROBO1*, OMIM 602430), or downregulated such as Slit Guidance Ligand 3 (*SLIT3*, OMIM 603745), semaphorin 4A (*SEMA4A*, OMIM 607292), tenascin C (*TNC*, OMIM 187380) and several ephrins (*EPHs*). DEGs associated with those categories were also downregulated at the NSC state, such as Unc-5 Netrin Receptor D (*UNC5D*, OMIM 616466), Growth Associated Protein 43 (*GAP43*, OMIM 162060), the ephrin Type-B Receptor 1 (*EPHB1*, OMIM 600600) or *TNC* (Figure S4B). Results were confirmed for a set of genes by qRT-PCR (Figure 4C). Altogether, these data suggest that a neurite outgrowth program is deregulated in WS neurons.

Taking into account the literature that associates degeneration processes in Wolfram with the activation of the Unfolded Protein Response (UPR)¹¹, we specifically analyzed the expression of selected UPR target genes. Under basal (and vehicle) condition no difference between CT and WS NSCs was detected (Figure S4C, D). In contrast, activation of the ER stress response by treating the cells with 50 nM thapsigargin (TG) revealed a slower return to baseline of the splicing of X Box-Binding protein 1 (*XBP1*, OMIM 194355) mRNA in WS than in CT, indicating

that WS cells could be more sensitive to ER stress (Figure 4D, E). These results suggest that UPR signaling might be affected in WS cells and may lead to chronic and low intensity signaling alterations resulting in turn into pathological phenotypes.

Pharmacological rescue of WS neurons and potential mechanisms of action

To test the latter hypothesis, we sought to investigate how the three branches of the UPR could contribute to the identified neuritic phenotype using selective pharmacological inhibitors. Using this approach, neither IRE1 α inhibition (using MKC-8866) nor alteration of the integrated stress response (ISR, using salubrinal) did elicit any change of the abnormal neuritic network of WS cells (Figure 5A, B, C, D, E, F and Figure S5A, B, C, D, E, F and G). In contrast, inhibition of the ATF6 α branch of the UPR using 10 μ M ceapin-A7 rescued neurites formation by WS cells during neuronal differentiation. Ceapin-A7 treated WS cell cultures showed neuritic networks that closely resembled CT cultures in terms both of the number of neuritic structures in the interval superior to 6 μ m of thickness (Figure 5G, H, I and Figure S5H, I, J) and of the mean thickness (2.162 \pm 0.256 μ m for NT vs 1.265 \pm 0.177 μ m for ceapin-A7). These results suggest the existence of non-conventional (non-acute) signaling ATF6 mechanisms in WS cells that may lead to aberrant neuritic structures and that are blunted by ceapin-A7.

Valproic acid treatment has positive effects on neurite outgrowth and axon guidance genes in WS neurons

In the same line of thought, the effects of various drugs that are currently being tested in individuals with WS or under preclinical study, namely the calcium modulator dantrolene, the GLP1 agonist liraglutide, the HDAC inhibitors 4-phenyl butyric acid (4PBA) and valproic acid (VPA, also described as an ER stress signaling attenuator), were evaluated on the pathological neurite outgrowth phenotype. Neuraminidase (NM) was used as a control as this enzyme reduces non-specific adhesion between neurites. Accordingly, 10 mU NM prevented the formation of fascicles in WS neurons when applied at the beginning of the post-mitotic neuronal differentiation (Figure 6A). NM had no effect on global genes expression. There was no

difference in neurite outgrowth defects between treated and non-treated WS cell cultures when using either 100 nM liraglutide, 1 mM 4-phenylbutyric acid or 10 μ M dantrolene (Figure S6A). In contrast, 1.5 mM VPA treated-WS cells demonstrated a change in the abnormal neuritic phenotype, displaying a profile comparable to those of NM-treated WS neurons (Figure 6A). WS neurons treated with that dose showed a neuritic network similar to CT neurons, in terms both of isolated and bundled fibers (Figure 6B, C, D and Figure S6B). In parallel, VPA increased the expression of *SLIT3*, *TNC* and *EPHB1*, three of the axon guidance genes that are downregulated in WS cells (Figure 6E). VPA had no impact on either the number of cells or the proportion of HuC/D+ neurons in the cultures, precluding a toxic effect (Figure S6C, D). In contrast, attempts at correcting the pathological phenotype after it was installed by starting the VPA treatment at DIV 18 were ineffective. As a search for additional clues concerning molecular mechanisms, VPA was tested for a protective effect on the prolonged thapsigargin-induced ER stress response observed in WS NSCs. There was no protection elicited by this drug. Valproic acid thus demonstrated a preventive effect on the neurite outgrowth abnormality observed in WS neurons, the mechanism of which is unrelated to a protection against an abnormal ER stress response.

DISCUSSION

The main result of the present study is the demonstration that human iPSC-derived neurons with Wolfram syndrome-associated mutations display phenotypic and molecular neurodevelopmental defects. This reveals as an alteration of the neuritic outgrowth and axonal pathfinding, together with abnormally extensive fasciculation in culture. Changes in gene expression concerned a set of genes involved in neurodevelopment and axonal pathfinding. It may be speculated that these pathological alterations participate to the reduction of brain volume in individual affected by WS. Although the expression of genes encoding proteins involved in the acute response to UPR was not altered, WS cells appeared more sensitive to ER stress. Among the currently explored therapeutic candidates, only valproic acid

demonstrated an ability at alleviating some of the observed neurodevelopmental defects in WS neurons.

The results of our study shed some light on a series of clinical results that appeared up to now paradoxical. Indeed, progressive neurodegenerative alteration pertaining to Wolfram syndrome that affect several neurosensory pathways^{2; 7; 25}, the brainstem and cerebellum^{5; 26} appear only several years after birth, in childhood and adolescence, and progress over time. However, these phenomena, that have dramatic clinical correlates, are preceded by an overall decrease in brain volume, both in grey and white matters, as recently demonstrated by a series of MRI studies^{3; 4}. These alterations were observed very early on in life and did not evolve with age, suggesting a neurodevelopmental defect previously ignored because it is clinically silent¹². Coherent with that observation, neurodevelopmental brain alteration were also observed in animal models of the disease²⁷⁻²⁹. Our *in vitro* cell culture results may well provide a mechanistic basis for those early neurodevelopmental alterations. Indeed, a proportion of WS neurons exhibited neurite outgrowth abnormalities that may make them unsuitable for elaborating normal sets of connections, ultimately being consequential for neuronal survival³⁰. Thick bundled neurites displayed trajectories that were not similar to those observed in CT cell cultures, extending over very long distances without apparent attraction towards cell bodies and forming curves or even full loops. Time-lapse imaging revealed a concomitant alteration of guiding cues at the tip of the bundled neurites. These phenotypic changes were coherently associated with a prevalent dysregulation of a set of genes that belong to the “axon guidance” subset. Among the most dysregulated genes were *SLIT3*, *SEMA4A*, *UNC5D5*, *TNC*, *GAP43*, *ROBO1* and several *EPHRINS*, that all encode proteins that are necessary for axonal pathfinding and whose defect is associated with major neurodevelopmental abnormalities^{31; 32}. Different studies have described a potential link between axonal pathfinding defects and reduced brain volume both in murine models and in persons³³⁻³⁶. The precise mechanisms by which the dysregulation of the expression of those genes may lead to reduced brain volumes in individuals with Wolfram syndrome remain however to be fully established.

Most of the dysregulated genes that are referred to above are encoding proteins either located at the plasma membrane or exerting their functions extracellularly. As such, they require functional biogenesis pathways, which encompass the secretory pathway. Interestingly, wolframin has been shown to act as a regulator of the ER homeostasis master regulator, namely the Unfolded Protein Response and pathological mechanisms associated to Wolfram syndrome have been largely ascribed to a defective control of those processes due to the loss of wolframin ¹⁰. In our model, there was no difference between the expression at baseline of any of the acute ER stress markers in neural cells derived from either CT or WS iPS cell lines, in contrast to what has been reported for pancreatic β cells ^{17; 37}. It is only when ER stress was elicited by thapsigargin that WS NSCs demonstrated a prolonged activation of *XBP1* mRNA splicing as compared to CT, thus indicative of a reduced ability of those cells to cope with prolonged ER stress. These results suggest that, even though under basal conditions canonical ER stress markers are not detected, ER homeostasis appears to be affected in WS neural cells. This hypothesis was confirmed when WS-associated phenotype was blunted upon treatment with ceapin-A7, an ATF6 inhibitor ³⁸. Since wolframin was shown to inhibit ATF6 activation ¹⁰, our results suggest that neurite development may be impacted on by a constitutive/chronic activation of ATF6 in WS cells that may lead to an alteration of both ER homeostasis and capacity to handle stress in those cells.

The observation of a clear pathological phenotype associated to altered gene expression markers in neural cells *in vitro* prompted us to analyze the potential therapeutic effects of drugs that are currently under pre-clinical or clinical study. The landscape of assayed treatments for Wolfram syndrome is, indeed, particularly rich, promoted by the observation of a number of potentially treatable functional defects ^{1; 39}. The demonstrated loss of calcium cell homeostasis ^{40; 41} has thus led to a clinical trial based upon the ER calcium stabilizer dantrolene (NCT02829268). In parallel, the nonselective histone deacetylase inhibitor valproic acid (VPA) is currently tested in clinical trial (NCT03717909) after been shown to reverse the defective production of P21^{cip} in *WFS1* knock-out cells ⁴². Other drugs under preclinical study include GLP1-agonists such as liraglutide that showed neuroprotective in Wolfram cell models in

addition to its expected effect on insulin secretion ^{43; 44}, and the chemical chaperone with anti-oxidant activity 4-PBA ³⁹. In our model, only VPA demonstrated a dose-dependent preventive action on the aberrant neurite outgrowth, and this was associated with the normalization of the expression of genes encoding axon guidance proteins. VPA has been shown to reduce ER stress ⁴⁵ and this may participate to its positive effects on WS neurons. Alternatively, one may hypothesize a less specific effect since VPA is a very potent non-specific histone deacetylase inhibitor that impacts well over one thousand genes in neural cells *in vitro* ⁴⁶. As a pleiotropic neuroactive drug, it is known to exert neuroprotective effects in a wide array of models of neurodegenerative diseases, including amyotrophic lateral sclerosis ⁴⁷, Parkinson's disease ⁴⁸ or spinal cord injury ⁴⁹. Of particular interest for the interpretation of our data are the results of two studies that explored the promotion of neurite outgrowth by VPA in two models of neural defects due to different CMT mutations, Rab7 in CMT2B ⁵⁰ and AARS in CMT2N ⁵¹. The fact that VPA appeared to promote neurite outgrowth in similar fashion in pathological models based on different gene mutations strongly suggest that those drug effects were not specific of a discrete pathological mechanism. Nevertheless, our data support the hypothesis that VPA may help alleviate some symptoms in individuals with Wolfram syndrome, which is currently tried in the clinic.

Whether the identified neurodevelopmental defects in axonal pathfinding may be associated after years with the observed neurodegenerative phenomena or whether neurodevelopmental and neurodegenerative processes are due to independent pathological mechanisms is at this stage but a matter of speculation. It is worth mentioning, however, that a link between such differentially timed defects has been hypothesized by several authors over the past ten years for other late-appearing neurodegenerative diseases. In a seminal review, Lin and co-workers ⁵² underlined the fact that genome-wide analyses for Parkinson disease revealed that single nucleotide polymorphisms in axon-guidance genes were predictive of different Parkinson's disease outcomes. This was further extended to other neurodegenerative diseases ⁵³ and, in particular, impaired axonal sprouting was hypothetically associated to dysregulation of axon guidance proteins in amyotrophic lateral sclerosis. Axonal pathfinding is

fundamental for the establishment of proper connectivity and functionality of neurons in the adult central nervous system. It has been proposed that dysregulation of developmental processes requiring axon guidance may be compensated to a certain point in time but later lead to degeneration⁵²⁻⁵⁵. Conversely, subtle defects in proteins that play a role not only during neurodevelopment but also in adult neuroplasticity may contribute to delayed neurodegeneration.

Supplemental Data

Supplemental data include 6 figures, 4 movies and 3 tables.

Acknowledgements

I-Stem is part of the Biotherapies Institute for Rare Diseases (BIRD) supported by the Association Française contre les Myopathies (AFM-Téléthon). This project was also supported by grants from Association syndrome de Wolfram, Association Nationale de la Recherche et de la Technologie and Agence Nationale pour la Recherche : NeurATRIS ANR-11-INBS-0011 and Labex REVIVE ANR-10-LABX-73. M.-G.B.-M. was supported by the programme “investissement d’avenir” INGESTEM. We thank Yolande Masson and Lina El Kassar for karyotyping the cell lines and Alexandre Carteron for the technical support with the ampliseq experiments. We thank Dr Cécile Delettre and the late Pr Christian Hamel (Institut des neurosciences de Montpellier) for the gift of the WS5 fibroblasts, and the New York Stem Cell Foundation for WS1 and WS2 iPSC lines. We thank Pr Ole Isacson (Harvard Medical School) for advice and reading the manuscript and Pr Nathalie Holic for advice with genome editing. We gratefully acknowledge support from the PSMN (Pôle Scientifique de Modélisation Numérique) of the ENS de Lyon for computing resource.

Declaration of Interests: The authors declare no competing interests.

Data and Code availability: The transcriptomic datasets generated during this study are available at NCBI GEO under the accession number GSE156911 (<https://www.ncbi.nlm.nih.gov/geo/query/acc.cgi?acc=GSE156911>).

WEB RESOURCES

<http://www.omim.org>

REFERENCES

1. Pallotta, M.T., Tascini, G., Crispoldi, R., Orabona, C., Mondanelli, G., Grohmann, U., and Esposito, S. (2019). Wolfram syndrome, a rare neurodegenerative disease: from pathogenesis to future treatment perspectives. *Journal of translational medicine* 17, 238.
2. Hershey, T., Lugar, H.M., Shimony, J.S., Rutlin, J., Koller, J.M., Perantie, D.C., Paciorkowski, A.R., Eisenstein, S.A., Permutt, M.A., and Washington University Wolfram Study, G. (2012). Early brain vulnerability in Wolfram syndrome. *PloS one* 7, e40604.
3. Lugar, H.M., Koller, J.M., Rutlin, J., Marshall, B.A., Kanekura, K., Urano, F., Bischoff, A.N., Shimony, J.S., Hershey, T., and Washington University Wolfram Syndrome Research Study, G. (2016). Neuroimaging evidence of deficient axon myelination in Wolfram syndrome. *Sci Rep* 6, 21167.
4. Lugar, H.M., Koller, J.M., Rutlin, J., Eisenstein, S.A., Neyman, O., Narayanan, A., Chen, L., Shimony, J.S., and Hershey, T. (2019). Evidence for altered neurodevelopment and neurodegeneration in Wolfram syndrome using longitudinal morphometry. *Sci Rep* 9, 6010.
5. Shannon, P., Becker, L., and Deck, J. (1999). Evidence of widespread axonal pathology in Wolfram syndrome. *Acta neuropathologica* 98, 304-308.
6. Chaussenot, A., Bannwarth, S., Rouzier, C., Vialettes, B., Mkadem, S.A., Chabrol, B., Cano, A., Labauge, P., and Paquis-Flucklinger, V. (2011). Neurologic features and genotype-phenotype correlation in Wolfram syndrome. *Annals of neurology* 69, 501-508.
7. Barrett, T.G., Bunday, S.E., and Macleod, A.F. (1995). Neurodegeneration and diabetes: UK nationwide study of Wolfram (DIDMOAD) syndrome. *Lancet* 346, 1458-1463.
8. Rohayem, J., Ehlers, C., Wiedemann, B., Holl, R., Oexle, K., Kordonouri, O., Salzano, G., Meissner, T., Burger, W., Schober, E., et al. (2011). Diabetes and neurodegeneration in Wolfram syndrome: a multicenter study of phenotype and genotype. *Diabetes care* 34, 1503-1510.
9. Takeda, K., Inoue, H., Tanizawa, Y., Matsuzaki, Y., Oba, J., Watanabe, Y., Shinoda, K., and Oka, Y. (2001). WFS1 (Wolfram syndrome 1) gene product: predominant subcellular localization to endoplasmic reticulum in cultured cells and neuronal expression in rat brain. *Human molecular genetics* 10, 477-484.
10. Fonseca, S.G., Ishigaki, S., Osowski, C.M., Lu, S., Lipson, K.L., Ghosh, R., Hayashi, E., Ishihara, H., Oka, Y., Permutt, M.A., et al. (2010). Wolfram syndrome 1 gene negatively regulates ER stress signaling in rodent and human cells. *The Journal of clinical investigation* 120, 744-755.
11. Fonseca, S.G., Fukuma, M., Lipson, K.L., Nguyen, L.X., Allen, J.R., Oka, Y., and Urano, F. (2005). WFS1 is a novel component of the unfolded protein response and maintains homeostasis of the endoplasmic reticulum in pancreatic beta-cells. *The Journal of biological chemistry* 280, 39609-39615.
12. Samara, A., Rahn, R., Neyman, O., Park, K.Y., Samara, A., Marshall, B., Dougherty, J., and Hershey, T. (2019). Developmental hypomyelination in Wolfram syndrome: new insights from neuroimaging and gene expression analyses. *Orphanet journal of rare diseases* 14, 279.
13. Chambers, S.M., Fasano, C.A., Papapetrou, E.P., Tomishima, M., Sadelain, M., and Studer, L. (2009). Highly efficient neural conversion of human ES and iPS cells by dual inhibition of SMAD signaling. *Nature biotechnology* 27, 275-280.
14. Boissart, C., Nissan, X., Giraud-Triboult, K., Peschanski, M., and Benchoua, A. (2012). miR-125 potentiates early neural specification of human embryonic stem cells. *Development* 139, 1247-1257.
15. Boissart, C., Poulet, A., Georges, P., Darville, H., Julita, E., Delorme, R., Bourgeron, T., Peschanski, M., and Benchoua, A. (2013). Differentiation from human pluripotent stem cells of cortical neurons of the superficial layers amenable to psychiatric disease modeling and high-throughput drug screening. *Translational psychiatry* 3, e294.

16. Darville, H., Poulet, A., Rodet-Amsellem, F., Chatrousse, L., Pernelle, J., Boissart, C., Heron, D., Nava, C., Perrier, A., Jarrige, M., et al. (2016). Human Pluripotent Stem Cell-derived Cortical Neurons for High Throughput Medication Screening in Autism: A Proof of Concept Study in SHANK3 Haploinsufficiency Syndrome. *EBioMedicine* 9, 293-305.
17. Shang, L., Hua, H., Foo, K., Martinez, H., Watanabe, K., Zimmer, M., Kahler, D.J., Freeby, M., Chung, W., LeDuc, C., et al. (2014). beta-cell dysfunction due to increased ER stress in a stem cell model of Wolfram syndrome. *Diabetes* 63, 923-933.
18. Yu, J., Hu, K., Smuga-Otto, K., Tian, S., Stewart, R., Slukvin, I., and Thomson, J.A. (2009). Human induced pluripotent stem cells free of vector and transgene sequences. *Science* 324, 797-801.
19. Hetz, C., Axten, J.M., and Patterson, J.B. (2019). Pharmacological targeting of the unfolded protein response for disease intervention. *Nature chemical biology* 15, 764-775.
20. Wakade, C.G., Mehta, S.H., Maeda, M., Webb, R.C., and Chiu, F.C. (2013). Axonal fasciculation and the role of polysialic acid-neural cell adhesion molecule in rat cortical neurons. *Journal of neuroscience research* 91, 1408-1418.
21. Li, W., Turner, A., Aggarwal, P., Matter, A., Storvick, E., Arnett, D.K., and Broeckel, U. (2015). Comprehensive evaluation of AmpliSeq transcriptome, a novel targeted whole transcriptome RNA sequencing methodology for global gene expression analysis. *BMC genomics* 16, 1069.
22. Amrhein, V., Greenland, S., and McShane, B. (2019). Scientists rise up against statistical significance. *Nature* 567, 305-307.
23. Chen, E.Y., Tan, C.M., Kou, Y., Duan, Q., Wang, Z., Meirelles, G.V., Clark, N.R., and Ma'ayan, A. (2013). Enrichr: interactive and collaborative HTML5 gene list enrichment analysis tool. *BMC bioinformatics* 14, 128.
24. Kuleshov, M.V., Jones, M.R., Rouillard, A.D., Fernandez, N.F., Duan, Q., Wang, Z., Koplev, S., Jenkins, S.L., Jagodnik, K.M., Lachmann, A., et al. (2016). Enrichr: a comprehensive gene set enrichment analysis web server 2016 update. *Nucleic acids research* 44, W90-97.
25. Carson, M.J., Slager, U.T., and Steinberg, R.M. (1977). Simultaneous occurrence of diabetes mellitus, diabetes insipidus, and optic atrophy in a brother and sister. *American journal of diseases of children* 131, 1382-1385.
26. Scolding, N.J., Kellar-Wood, H.F., Shaw, C., Shneerson, J.M., and Antoun, N. (1996). Wolfram syndrome: hereditary diabetes mellitus with brainstem and optic atrophy. *Annals of neurology* 39, 352-360.
27. Cagalinec, M., Liiv, M., Hodurova, Z., Hickey, M.A., Vaarmann, A., Mandel, M., Zeb, A., Choubey, V., Kuum, M., Safiulina, D., et al. (2016). Role of Mitochondrial Dynamics in Neuronal Development: Mechanism for Wolfram Syndrome. *PLoS biology* 14, e1002511.
28. Plaas, M., Seppa, K., Reimets, R., Jagomae, T., Toots, M., Koppel, T., Vallisoo, T., Nigul, M., Heinla, I., Meier, R., et al. (2017). Wfs1- deficient rats develop primary symptoms of Wolfram syndrome: insulin-dependent diabetes, optic nerve atrophy and medullary degeneration. *Sci Rep* 7, 10220.
29. Sakakibara, Y., Sekiya, M., Fujisaki, N., Quan, X., and Iijima, K.M. (2018). Knockdown of wfs1, a fly homolog of Wolfram syndrome 1, in the nervous system increases susceptibility to age- and stress-induced neuronal dysfunction and degeneration in *Drosophila*. *PLoS genetics* 14, e1007196.
30. Zweifel, L.S., Kuruvilla, R., and Ginty, D.D. (2005). Functions and mechanisms of retrograde neurotrophin signalling. *Nature reviews Neuroscience* 6, 615-625.
31. Wang, L., and Marquardt, T. (2013). What axons tell each other: axon-axon signaling in nerve and circuit assembly. *Current opinion in neurobiology* 23, 974-982.
32. Roig-Puiggros, S., Vigouroux, R.J., Beckman, D., Bocai, N.I., Chiou, B., Davimes, J., Gomez, G., Grassi, S., Hoque, A., Karikari, T.K., et al. (2020). Construction and reconstruction of brain circuits: normal and pathological axon guidance. *J Neurochem* 153, 10-32.
33. Engle, E.C. (2010). Human genetic disorders of axon guidance. *Cold Spring Harbor perspectives in biology* 2, a001784.

34. Hibar, D.P., Stein, J.L., Jahanshad, N., Kohannim, O., Hua, X., Toga, A.W., McMahon, K.L., de Zubicaray, G.I., Martin, N.G., Wright, M.J., et al. (2015). Genome-wide interaction analysis reveals replicated epistatic effects on brain structure. *Neurobiology of aging* 36 Suppl 1, S151-158.
35. Vosberg, D.E., Zhang, Y., Menegaux, A., Chalupa, A., Manitt, C., Zehntner, S., Eng, C., DeDuck, K., Allard, D., Durand, F., et al. (2018). Mesocorticolimbic Connectivity and Volumetric Alterations in DCC Mutation Carriers. *The Journal of neuroscience : the official journal of the Society for Neuroscience* 38, 4655-4665.
36. Deloulme, J.C., Gory-Faure, S., Mauconduit, F., Chauvet, S., Jonckheere, J., Boulan, B., Mire, E., Xue, J., Jany, M., Maucier, C., et al. (2015). Microtubule-associated protein 6 mediates neuronal connectivity through Semaphorin 3E-dependent signalling for axonal growth. *Nature communications* 6, 7246.
37. Urano, F. (2014). Wolfram syndrome iPS cells: the first human cell model of endoplasmic reticulum disease. *Diabetes* 63, 844-846.
38. Gallagher, C.M., and Walter, P. (2016). Ceapins inhibit ATF6alpha signaling by selectively preventing transport of ATF6alpha to the Golgi apparatus during ER stress. *eLife* 5.
39. Abreu, D., and Urano, F. (2019). Current Landscape of Treatments for Wolfram Syndrome. *Trends in pharmacological sciences* 40, 711-714.
40. Lu, S., Kanekura, K., Hara, T., Mahadevan, J., Spears, L.D., Osowski, C.M., Martinez, R., Yamazaki-Inoue, M., Toyoda, M., Neilson, A., et al. (2014). A calcium-dependent protease as a potential therapeutic target for Wolfram syndrome. *Proceedings of the National Academy of Sciences of the United States of America* 111, E5292-5301.
41. Cagalinec, M., Zahradnikova, A., Zahradnikova, A., Jr., Kovacova, D., Paulis, L., Kurekova, S., Hot'ka, M., Pavelkova, J., Plaas, M., Novotova, M., et al. (2019). Calcium Signaling and Contractility in Cardiac Myocyte of Wolframin Deficient Rats. *Frontiers in physiology* 10, 172.
42. Gharanei, S., Zatyka, M., Astuti, D., Fenton, J., Sik, A., Nagy, Z., and Barrett, T.G. (2013). Vacuolar-type H⁺-ATPase V1A subunit is a molecular partner of Wolfram syndrome 1 (WFS1) protein, which regulates its expression and stability. *Human molecular genetics* 22, 203-217.
43. Kondo, M., Tanabe, K., Amo-Shiinoki, K., Hatanaka, M., Morii, T., Takahashi, H., Seino, S., Yamada, Y., and Tanizawa, Y. (2018). Activation of GLP-1 receptor signalling alleviates cellular stresses and improves beta cell function in a mouse model of Wolfram syndrome. *Diabetologia* 61, 2189-2201.
44. Seppa, K., Toots, M., Reimets, R., Jagomae, T., Koppel, T., Pallase, M., Hasselholt, S., Krogsbaek Mikkelsen, M., Randel Nyengaard, J., Vasar, E., et al. (2019). GLP-1 receptor agonist liraglutide has a neuroprotective effect on an aged rat model of Wolfram syndrome. *Sci Rep* 9, 15742.
45. Li, Z., Wu, F., Zhang, X., Chai, Y., Chen, D., Yang, Y., Xu, K., Yin, J., Li, R., Shi, H., et al. (2017). Valproate Attenuates Endoplasmic Reticulum Stress-Induced Apoptosis in SH-SY5Y Cells via the AKT/GSK3beta Signaling Pathway. *International journal of molecular sciences* 18.
46. Fukuchi, M., Nii, T., Ishimaru, N., Minamino, A., Hara, D., Takasaki, I., Tabuchi, A., and Tsuda, M. (2009). Valproic acid induces up- or down-regulation of gene expression responsible for the neuronal excitation and inhibition in rat cortical neurons through its epigenetic actions. *Neuroscience research* 65, 35-43.
47. Wang, X., Ma, M., Teng, J., Che, X., Zhang, W., Feng, S., Zhou, S., Zhang, Y., Wu, E., and Ding, X. (2015). Valproate Attenuates 25-kDa C-Terminal Fragment of TDP-43-Induced Neuronal Toxicity via Suppressing Endoplasmic Reticulum Stress and Activating Autophagy. *International journal of biological sciences* 11, 752-761.
48. Harrison, I.F., Crum, W.R., Vernon, A.C., and Dexter, D.T. (2015). Neurorestoration induced by the HDAC inhibitor sodium valproate in the lactacystin model of Parkinson's is associated with histone acetylation and up-regulation of neurotrophic factors. *British journal of pharmacology* 172, 4200-4215.

49. Chu, T., Zhou, H., Lu, L., Kong, X., Wang, T., Pan, B., and Feng, S. (2015). Valproic acid-mediated neuroprotection and neurogenesis after spinal cord injury: from mechanism to clinical potential. *Regenerative medicine* 10, 193-209.
50. Yamauchi, J., Torii, T., Kusakawa, S., Sanbe, A., Nakamura, K., Takashima, S., Hamasaki, H., Kawaguchi, S., Miyamoto, Y., and Tanoue, A. (2010). The mood stabilizer valproic acid improves defective neurite formation caused by Charcot-Marie-Tooth disease-associated mutant Rab7 through the JNK signaling pathway. *Journal of neuroscience research* 88, 3189-3197.
51. Tatsumi, Y., Matsumoto, N., Iibe, N., Watanabe, N., Torii, T., Sango, K., Homma, K., Miyamoto, Y., Sakagami, H., and Yamauchi, J. (2019). CMT type 2N disease-associated AARS mutant inhibits neurite growth that can be reversed by valproic acid. *Neuroscience research* 139, 69-78.
52. Lin, L., Lesnick, T.G., Maraganore, D.M., and Isacson, O. (2009). Axon guidance and synaptic maintenance: preclinical markers for neurodegenerative disease and therapeutics. *Trends Neurosci* 32, 142-149.
53. Van Battum, E.Y., Brignani, S., and Pasterkamp, R.J. (2015). Axon guidance proteins in neurological disorders. *The Lancet Neurology* 14, 532-546.
54. Stoeckli, E. (2017). Where does axon guidance lead us? *F1000Research* 6, 78.
55. Schwamborn, J.C. (2018). Is Parkinson's Disease a Neurodevelopmental Disorder and Will Brain Organoids Help Us to Understand It? *Stem cells and development* 27, 968-975.

FIGURE TITLES AND LEGENDS

Figure 1: WS and CT iPSCs both efficiently generate homogeneous populations of neural stem cells and neurons. **A.** Immunofluorescence microscopy for NESTIN (NSCs marker) and Ki67 (proliferation marker) in NSCs derived from the three control (CT1, CT2 and CT3) and the three WS (WS1, WS2, WS5) iPSC lines. Scale bars, 100 μ m. **B.** HuC/D and CUX2-immunoreactive cortical neurons at days of *in vitro* (DIV) differentiation 14 from NSC stage. Scale bars, 100 μ m. **C.** Proportion of HuC/D⁺ and CUX2⁺-immunoreactive neurons in cell culture at DIV 14 from NSC stage. Data are presented as mean \pm s.e.m. (n = 3 biologically independent differentiations. No statistical difference was observed using one-way ANOVA with Dunnett's post hoc test). **D.** Western blot of wolframin in NSCs and neurons at DIV 21.

Figure 2: WS neurons display abnormal neurite outgrowth. **A.** TUJ1-immunoreactive CT and WS neurons at DIV 21. Scale bars, 100 μ m. **B.** Confocal analysis of TUJ1-immunoreactive WS5 neurons at DIV 21. Scale bars, 10 μ m. **C.** Quantification of the mean thickness of isolated and bundled neurites in CT and WS neurons. **D.** Quantification of the number of isolated and bundled neurites per mm² over three thickness intervals (0 - 3; 3 - 6 and > 6 μ m) for CT and WS neurons (see methods). **E.** Quantification of the mean number of isolated and bundled neurites for CT and WS neurons in the > 6 μ m interval of thickness. The color code indicating the different cell lines is common to c, d, and e. All the data are presented as mean \pm s.e.m. (n = 3 biologically independent differentiations; **p < 0.01, ***p < 0.001; Student's t-test).

Figure 3: WFS1 cDNA knock-in rescues phenotype in WS neurons at DIV21. **A.** Gene editing strategy using CRISPR-Cas9 technology for insertion at the AAVS1 locus of *WFS1* cDNA under a doxycycline inducible promoter in WS5 iPSC line. **B.** Western blot detection of wolframin in rescued WS5 (WS5R) NSCs and neurons with or without doxycycline (Dox) treatment and in CT2. **C.** HuC/D and CUX2 immunostaining of WS5R neurons treated or not with Dox. Scale bars, 100 μ m. **D.** Proportion of HuC/D⁺ and CUX2⁺-immunoreactive cells in WS5R neurons treated or not with Dox. Data are presented as mean \pm s.e.m. (n = 3 biologically independent differentiations; Student's t-test). **E.** TUJ1 and HuC/D immunoreactive WS5R neurons treated or not with Dox. Scale bars, 100 μ m. **F.** Quantification of the mean thickness of isolated and bundled neurites for WS5R neurons treated or not with Dox compared to CT1. **G.** Quantification of the number of isolated and bundled neurites per mm² for three thickness intervals (0 - 3; 3 - 6 and > 6 μ m) in neurons. **H.** Analysis of the number of isolated and bundled neurites per mm² for the > 6 μ m interval in WS5R neurons treated or not with Dox compared to CT1. For f, g and h, data are expressed relative to that of CT1 cells and presented as mean \pm s.e.m. (n=3 for CT1 and n=4 for WS5R and WSR5 + Dox biologically independent differentiations; ***p < 0.001; one-way ANOVA with Dunnett's post hoc test, data are compared to CT1 cells).

Figure 4: Global gene expression comparison between CT and WS NSCs and neurons. **A and B.** Transcriptome analysis using AmpliSeq. **A.** Principal component analysis (PCA), between CT and WS

NSCs and neurons. **B.** KEGG pathways (upper panel) and gene ontology (lower panel) enrichment analysis in neurons using Enrichr tool. **C.** Quantitative RT-PCR analysis of DEGs mRNA levels in CT and WS NSCs and neurons. Data are expressed relative to that of CT1 cells and normalized to 18S rRNA expression. Data are presented as mean \pm s.e.m. (n = 3 biologically independent differentiations; ***p < 0.001; Student's t-test). **D and E.** ER stress induction in CT and WS NSCs after 4, 6 and 8 hours of 50 nM thapsigargin (TG) treatment. **D.** Analysis of the expression of spliced (*XBP1s*) and unspliced (*XBP1u*) *XBP1*. **E.** Quantification of *XBP1s* expression normalized to total *XBP1* (*XBP1t*). Data are presented as mean \pm s.e.m. (n = 3 biologically independent experiments; *p<0.05; one-way ANOVA with Dunnett's post hoc test).

Figure 5: Effect of the inhibition of each of the three branches of UPR pathways on the neurite outgrowth defect in WS5 neurons. A, B and C. Inhibition of IRE1 α pathway with 2.5 μ M MKC-8866 (MKC). **A.** TUJ1 and HuC/D immunostaining of WS5 neurons at DIV 18 after MKC or control DMSO treatments. Scale bars, 100 μ m. **B.** Quantification of the number of isolated and bundled neurites per mm² for three thickness intervals (0 - 3; 3 - 6 and > 6 μ m) in WS5 neurons treated or not with MKC or control DMSO. **C.** Quantification of the number of isolated and bundled neurites for the > 6 μ m interval in WS5 neurons treated or not with MKC or control DMSO. **D, E and F.** Same representation for the inhibition of integrated stress response with 10 μ M salubrinal. **G, H and I.** Same representation for the inhibition of ATF6 pathway using 10 μ M ceapin-A7. For all analyses, data are presented as mean \pm s.e.m. (n = 3 biologically independent differentiations; *p<0.05; one-way ANOVA with Dunnett's post hoc test, data are compared to non-treated cells (NT)).

Figure 6: Valproic Acid (VPA) treatment prevents abnormal neurite outgrowth in WS neurons. A. TUJ1 and HuC/D immunostaining of WS2 and WS5 neurons at DIV 18 without (NT) or after 0.5 or 1.5 mM VPA or 10 mU neuraminidase (NM) treatment. Scale bars, 100 μ m. **B.** Quantification of the number of isolated and bundled neurites per mm² for three thickness intervals (0 - 3; 3 - 6 and > 6 μ m) in WS2 and WS5 neurons treated or not with 0.5 or 1.5 mM VPA or 10 mU NM. **C.** Quantification of the number of isolated and bundled neurites for the > 6 μ m interval in WS2 and WS5 neurons treated or not with 0.5 or 1.5 mM VPA or 10 mU NM. **D.** Quantification of the mean thickness of isolated and bundled neurites for WS2 and WS5 neurons treated or not with 0.5 or 1.5 mM VPA or 10 mU NM. For b, c and d, data are expressed relative to that of CT2 cells. **E.** Quantitative RT-PCR analysis of *SLIT3*, *TNC* and *EPHB1* transcript levels in WS2 and WS5 neurons treated with 0.5 or 1.5 mM VPA. Data are expressed relative to that of non-treated cells (NT) and normalized to 18S rRNA expression. For all analyses, data are presented as mean \pm s.e.m. (n = 3 biologically independent differentiations; *p<0.05, **p < 0.01, ***p < 0.001; one-way ANOVA with Dunnett's post hoc test, data are compared to CT2 cells).

Supplemental movies legend: Time analysis of the neuronal network formation for CT and WS cells. a, b, c and d. Live-cell imaging of the neuronal network development of CT1 (a), WS1 (b), WS2 (c) and WS5 (d) neurons during 27 days of differentiation *in vitro* from NSC stage.

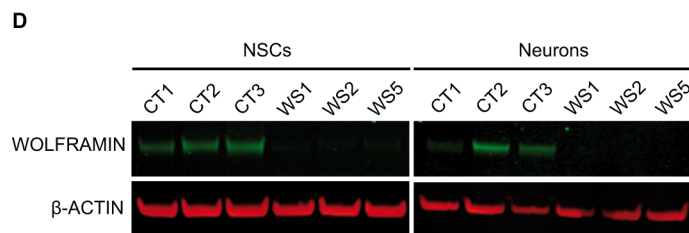
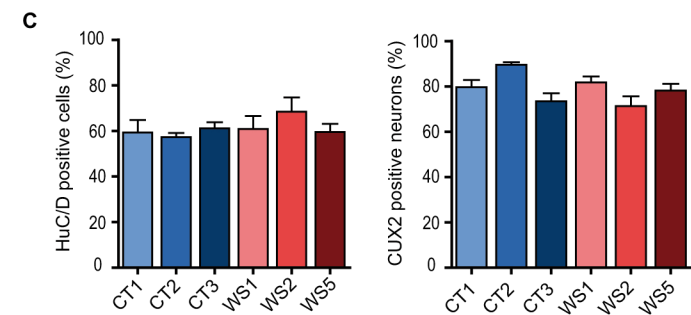
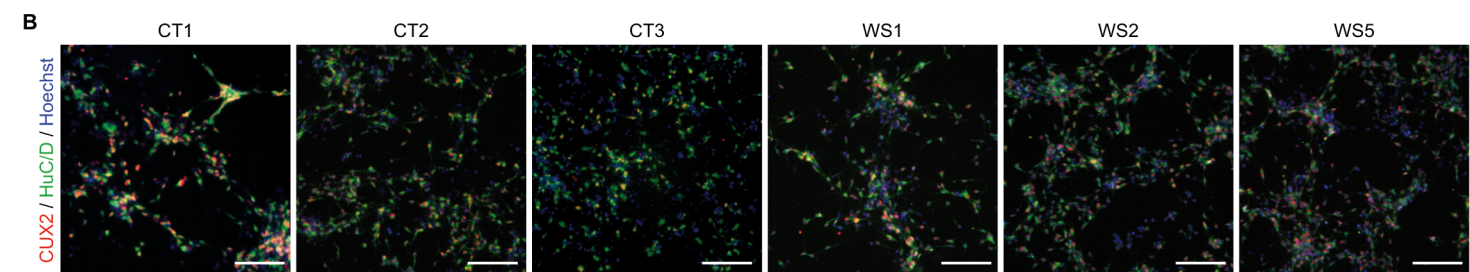
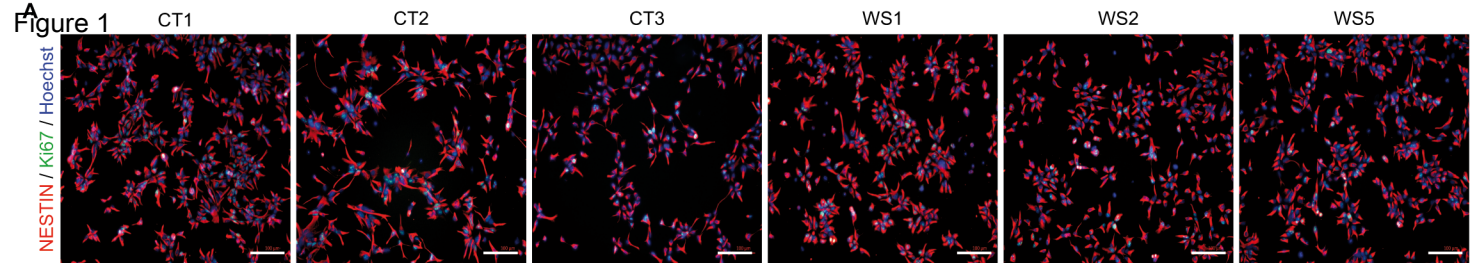
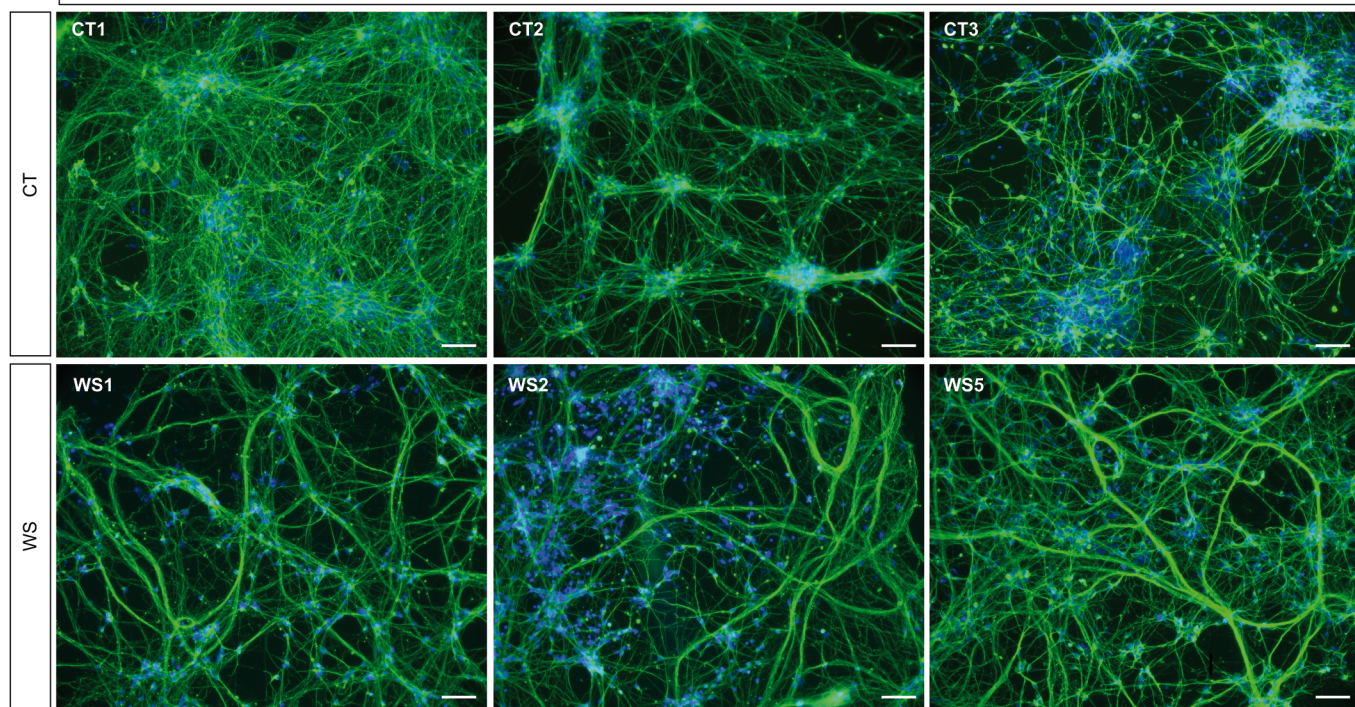
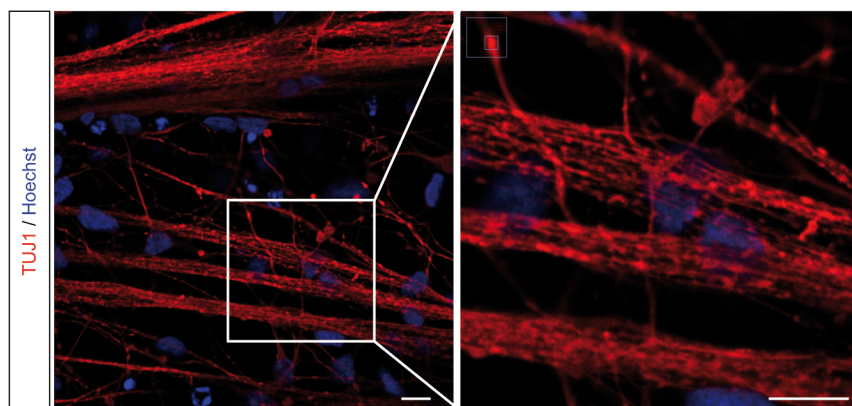


Figure 2

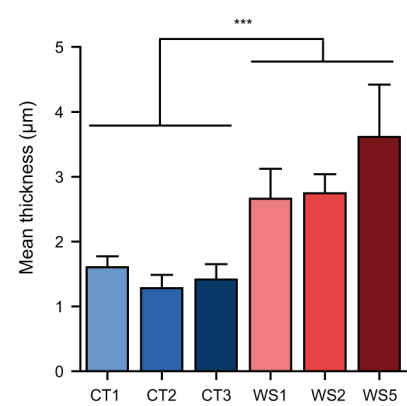
TUJ1 / Hoechst



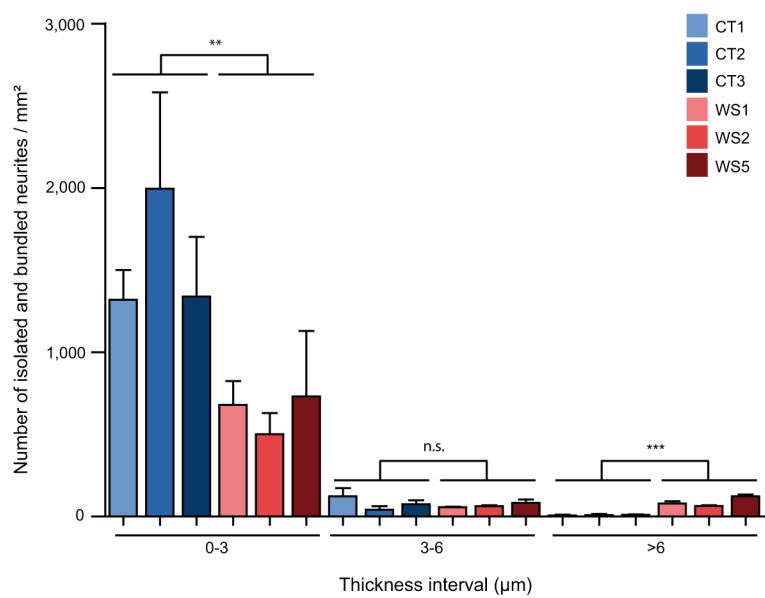
B



C



D



E

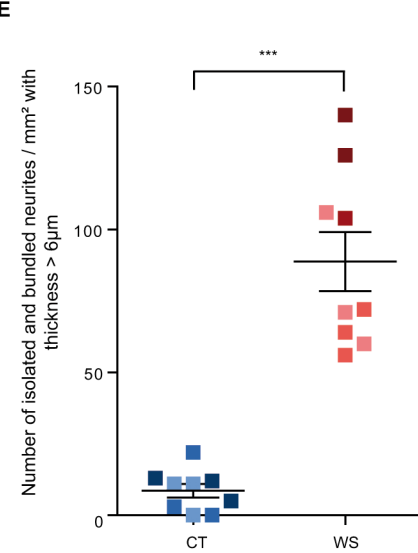
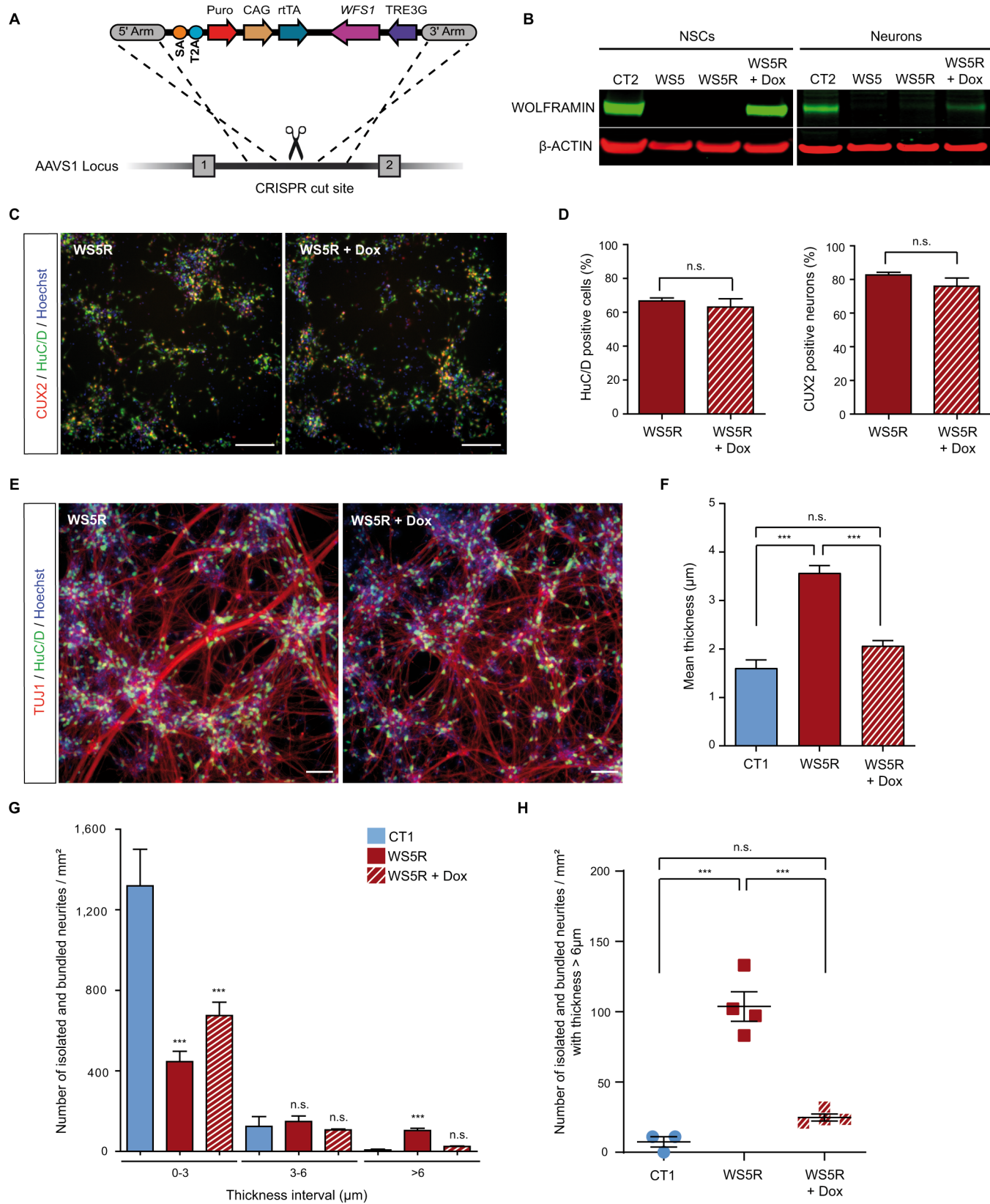


Figure 3



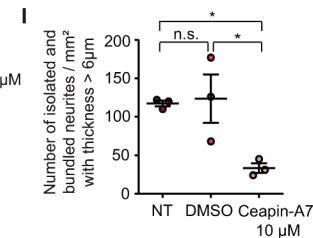
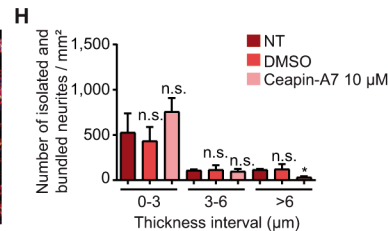
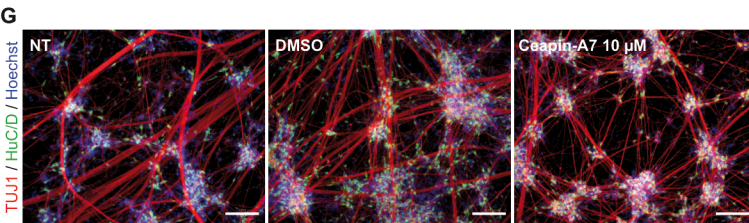
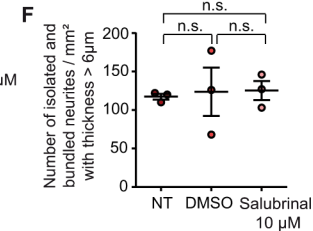
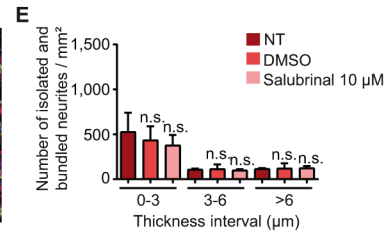
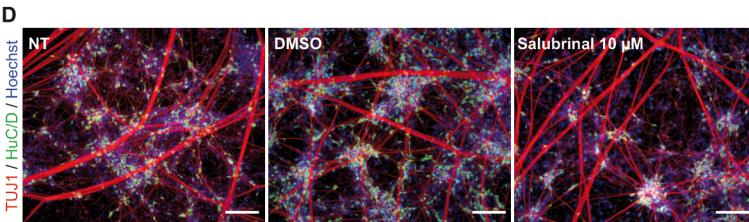
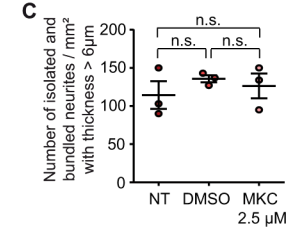
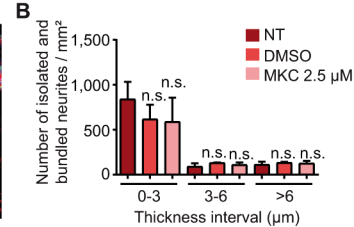
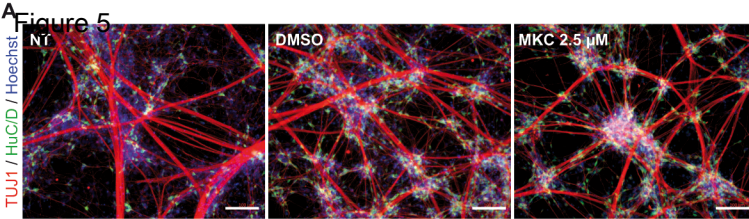


Figure 4

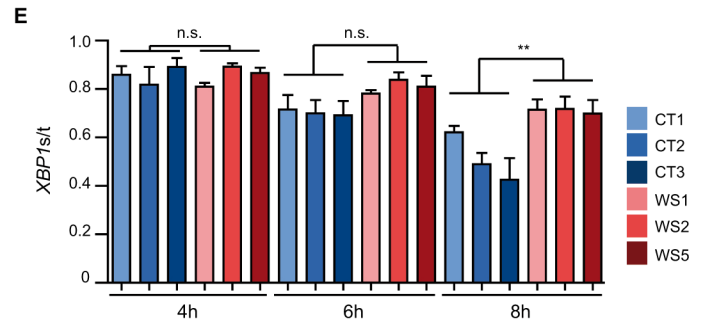
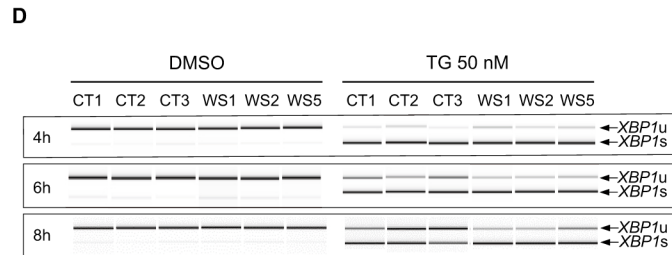
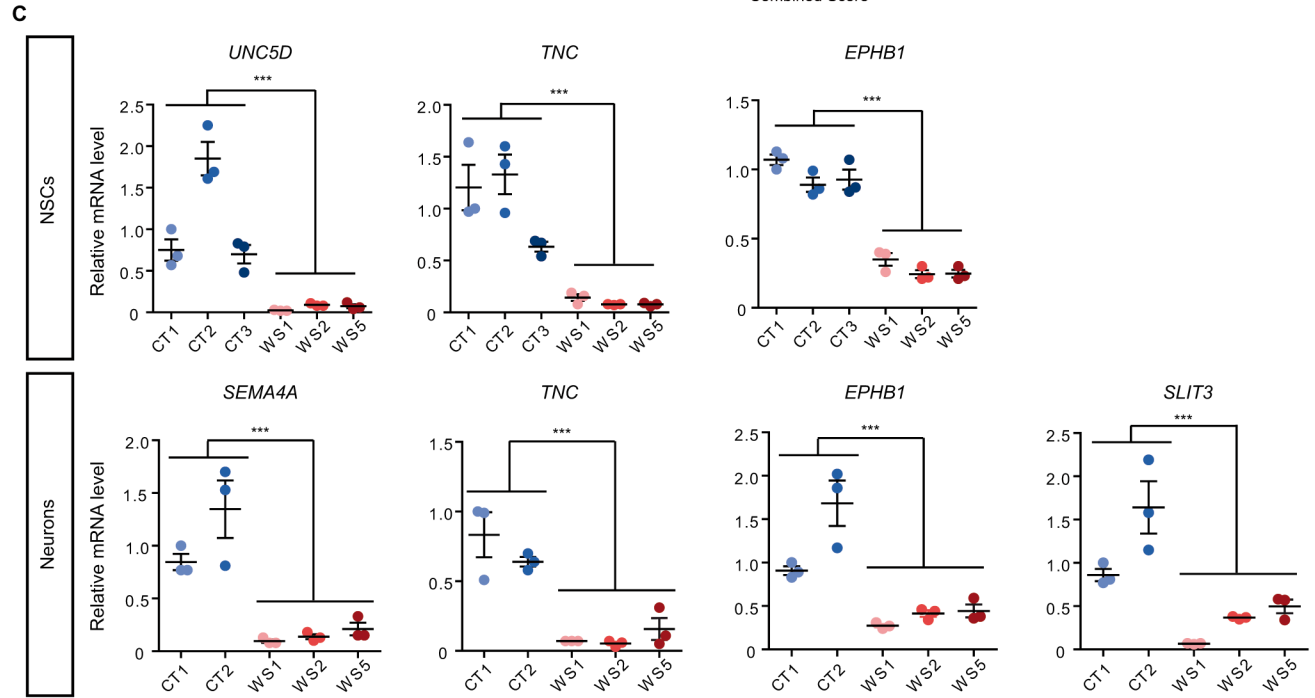
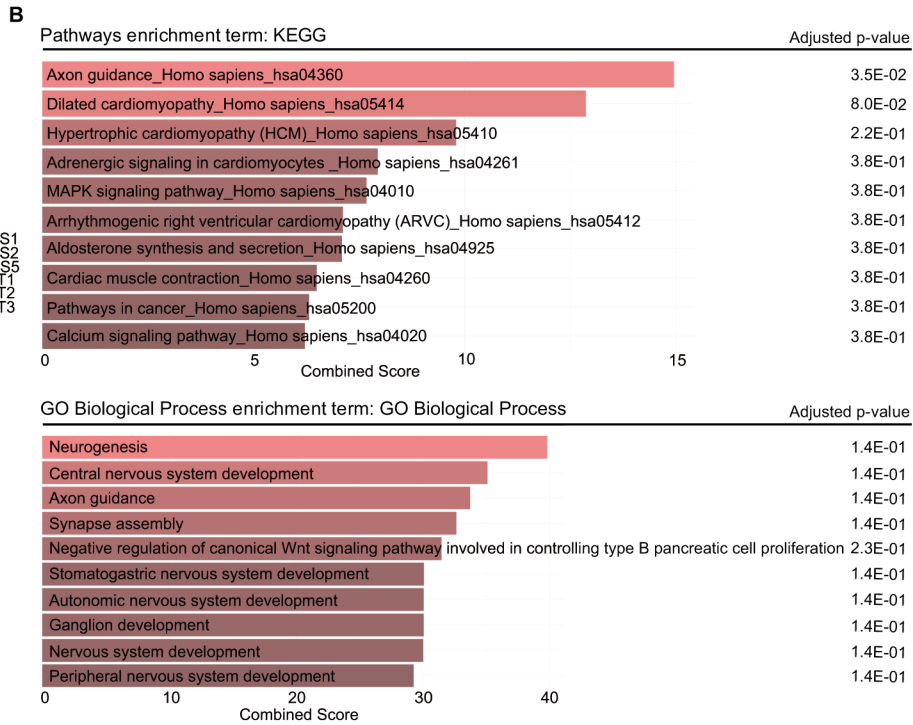
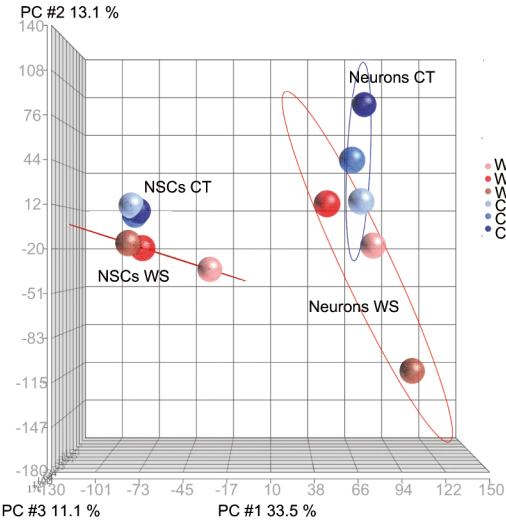
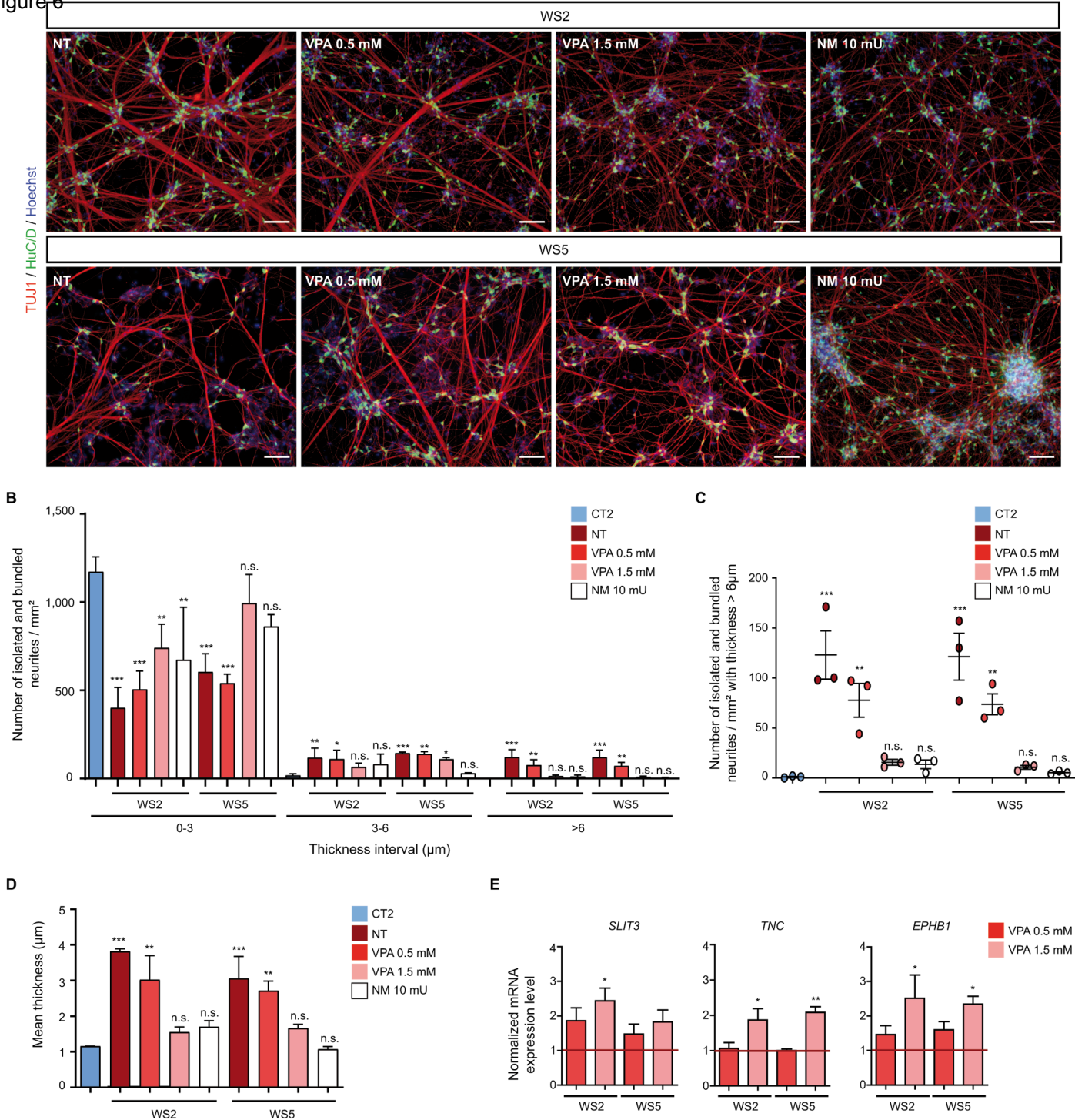


Figure 6





[Click here to access/download](#)

Supplemental Text and Figures

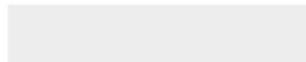
[Pourtoy-Brasselet_et_al_Supplemental_Data.pdf](#)





[Click here to access/download](#)

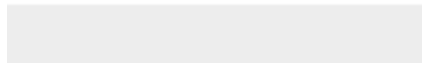
Supplemental Movies and Spreadsheets
Supplementary_movie_a_CT1.mp4





[Click here to access/download](#)

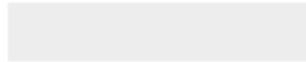
Supplemental Movies and Spreadsheets
Supplementary_movie_b_WS1.mp4





[Click here to access/download](#)

Supplemental Movies and Spreadsheets
Supplementary_movie_c_WS2.mp4





[Click here to access/download](#)

Supplemental Movies and Spreadsheets
Supplementary_movie_d_WS5.mp4

